

On the Aerodynamic Stability of Helicopter Rotor Wakes

Mahendra J. Bhagwat*

J. Gordon Leishman†

Alfred Gessow Rotorcraft Center,
Department of Aerospace Engineering,
Glenn L. Martin Institute of Technology,
University of Maryland, College Park, Maryland 20742

Abstract

An eigenvalue analysis has been developed to study the stability of helicopter rotor wakes in hover and axial flight. The results are supported with observed trends from hovering rotor wake experiments. The rotor wake is shown to be intrinsically unstable, with the tip vortices exhibiting several possible unstable deformation modes. The wake divergence (instability) rate associated with each deformation mode depends on the relative phase of the perturbations produced on tip vortex filaments generated by different blades. Wake divergence rates increase sharply after the initial radial contraction of the wake below the rotor, and is confirmed by experimental observations. The divergence rates are governed by the vortex-induced velocities; the divergence rate for any deformation mode decreases with increasing rotor thrust, and also with increasing climb rate. The so-called tip vortex ‘pairing’ phenomenon, sometimes empirically observed in hovering flight conditions, is shown to be a particular unstable long-wave deformation mode of the rotor wake. It is further shown that in numerical solutions of the wake using free-vortex wake methods this deformation mode can be artificially excited by numerical errors. A proper choice of numerical time integration algorithm is necessary to prevent non-physical growth of these numerical errors.

Nomenclature

c	Rotor blade chord, m
C_T	Rotor thrust coefficient, $T/(\rho\pi\Omega^2R^4)$
N	Number of helical vortex filaments
N_b	Number of blades
p	Helical pitch angle, rad
R	Rotor radius, m

*Graduate Research Assistant.

†Associate Professor.

Presented at the *American Helicopter Society 56th Annual Forum*, Virginia Beach, VA, May 2–4, 2000. Copyright ©2000 by the American Helicopter Society. All rights reserved.

r_c	Vortex core radius, m
r, θ, z	Cylindrical polar coordinates
\vec{r}	Position vector of a wake collocation point
t	Time, s
\vec{V}	Velocity vector at a wake collocation point
x, y, z	Cartesian coordinates
α	Divergence rate, s^{-1}
$\bar{\alpha}$	Non-dimensional divergence rate, $\alpha/(\Gamma_v/4\pi R^2)$
$\delta\vec{r}$	Wake geometry perturbation, m
Γ_v	Tip vortex circulation strength, m^2s^{-1}
Ω	Rotor rotational speed, $rads^{-1}$
ω	Wave number for a normal mode
ψ	Azimuth angle, rad
ψ_b	Blade azimuthal location, rad
σ	Rotor solidity, $N_b c/\pi R$
ζ	Vortex age, rad

Abbreviations

LHS	Left-Hand Side
RHS	Right-Hand Side
PIPC	Pseudo-Implicit Predictor-Corrector
PCC	Predictor-Corrector with Central difference
PC2B	Predictor-Corrector with 2 nd -order Backward difference
RMS	Root-Mean-Square
TPP	Tip Path Plane

Introduction

An improved understanding of the physical nature of the vortical wake is, perhaps, the most important factor in accurately predicting the aerodynamics of helicopter rotors. Accurate prediction of the non-uniform wake-induced inflow and the resulting blade loading is the key to improved levels of helicopter aeromechanics and flight dynamics analyses. The acoustic analysis of the rotor also requires high fidelity predictions of the rotor blade tip vortex trajectories and strengths. It is the inability to fully understand and model the tip vortices and the rotor wake that

limits the ability to design newer helicopters with better efficiency, lower vibration, and reduced rotor noise levels.

One problem that adversely influences rotor wake prediction capability is the inability to faithfully model the various types of wake disturbances and instabilities that have been observed in rotor experiments. These effects can be both global (i.e., affecting the total wake structure), as well as local (i.e., confined to only a small part of the tip vortex filaments). In some cases local wake instabilities can lead to vortex bursting, which is also poorly understood and difficult to model (e.g., Ref. 1). Global wake instabilities in a helicopter rotor wake can result from local interactions between closely spaced tip vortices. Wake instabilities and aperiodic wake formation often have their source in ‘pairing’ or localized roll-up between two adjacent tip vortex filaments. These effects were first observed in experiments with hovering rotors by Landgrebe (Ref. 2) and by Tangler *et al.* (Ref. 3). The phenomenon was attributed to an inherent characteristic of the vortical wake structure, which was supported by theoretical stability analyses of an infinitely long helical filament (Refs. 4, 5). Gupta & Loewy (Ref. 6) extended this stability analysis to multiple interdigitated helical vortices to examine multi-bladed rotor wakes. These studies have suggested, although only by analogy to infinite helical vortex filaments, that a hovering helicopter rotor wake is intrinsically unstable with several possible instability modes.

Recently, periodic interactions between tip vortex filaments in the form of vortex pairing have been empirically documented by Martin *et al.* (Ref. 7) and Caradonna *et al.* (Refs. 8, 9). While the pairing phenomenon is interesting, it is not a new observation, nor is it a general characteristic of the wake found with all rotor configurations. Experimental evidence suggests that the susceptibility of the rotor wake to pairing or other instabilities is affected by the number of blades and rotor operating state. In particular, with increasing thrust (or, alternatively, increasing collective pitch) the vortex pairing occurs at increasing downstream distance below the rotor (Ref. 3). A similar effect was reported with increasing climb velocity in Refs. 8 and 9. While the analysis of Gupta & Loewy (Ref. 6) would suggest that this vortex pairing is a form of wake instability, others have suggested otherwise. Jain *et al.* (Ref. 10) suggest that vortex pairing in rotor wakes is not an instability, but is a result of mutual interactions of two vortex filaments in a form that is analogous to the perpetual leap-frogging motion of two inviscid vortex rings. It could be further argued that the steady, deterministic nature of the wake trajectories observed in some of these recent experiments cannot be an inherent wake instability, mainly because instabilities are more often attributed to stochastic phenomena such as an overall aperiodicity of the rotor wake (Ref. 11).

Clearly, these empirical observations pose considerable challenges to the rotor analyst. From a rotor wake prediction standpoint, the highly periodic, repeatable nature of the wake visualization results observed by Martin *et al.* (Ref. 7) and Caradonna *et al.* (Refs. 8, 9) suggests that deterministic, first-principle based wake prediction methods should be able to model the tip vortex pairing process. In fact, some vortex wake methods seem to predict a behavior that closely replicates the vortex pairing that has been observed in experiments – see Refs. 10 and 12. However, the fact that some but not all prediction methods show this behavior raises some questions as to whether these effects have their source in the numerical methods themselves, rather than being physical in origin. Furthermore, the fact that the effects are present in some (almost identical) rotor experiments but not others suggests it is possible that the experimental setup, or flow turbulence and other recirculation in the test facility may be responsible for part, if not all, of the observed behavior of the wake. From a wake prediction standpoint, the most important question this raises is whether or not predictions that provide periodic wake geometries can be considered as equilibrium, steady-state solutions. It is also not immediately obvious as to why, in general, only time-accurate wake solutions are able to properly model this ‘inherent’ physics of interacting tip vortex filaments in the rotor wake.

In the present work, the wake behavior of a helicopter rotor in axial flight is introduced using numerical solutions to the wake problem using free-vortex schemes. These results are also supported using experimental measurements as a reference. It is further shown that the results obtained with free-vortex schemes are dependent on the numerical scheme used to solve the wake equations. Round-off and truncation errors can be responsible for the onset of wake instabilities, which in some cases may fortuitously replicate the observed physical behavior of the rotor wake. The problem is then approached rigorously using a linearized stability analysis that is applicable to any general rotor wake structure. Both the stability of an equilibrium wake geometry and its instability modes are examined to understand the source of mutual tip vortex interactions observed in both rotor experiments and in numerical solutions of the wake.

Numerical Wake Model

The general problem of rotor wake behavior and wake instabilities is first introduced with a numerical rotor wake model using free-vortex methods. Free-vortex wake methods have emerged as popular aerodynamic models for helicopter rotor analyses because they offer high fidelity and versatility at modest computational costs. These

methods can be categorized into two main types: time-accurate algorithms, where the wake governing equations are integrated in time (Refs. 13–19), and steady-state solution algorithms, which solve for a periodic solution either directly (Ref. 20), or by using relaxation approach (Refs. 21–26).

Free-vortex wake methods follow a Lagrangian approach and in the interest of computational economy, model the rotor wake using only the most dominant features — the blade tip vortices. The force-free motion of the tip vortices is governed by the vorticity transport theorem, which states that vorticity is transported along with the fluid. Thus, the motion of a point on a vortex filament is governed by the equation governing the motion of a fluid particle, i.e.,

$$\frac{d\vec{r}}{dt} = \vec{V}(\vec{r}) \quad (1)$$

where \vec{r} is the position vector of the point on the vortex filament and $\vec{V}(\vec{r})$ is the local fluid velocity at the point \vec{r} resulting from any external ‘free-stream’ velocity as well as induced velocities from the vortical wake structure. In a blade-fixed coordinate system, Eq. 1 can be written in the form of a partial differential equation as

$$\frac{\partial \vec{r}}{\partial \psi} + \frac{\partial \vec{r}}{\partial \zeta} = \frac{\vec{V}(\vec{r})}{\Omega} \quad (2)$$

where ψ is the azimuthal location of the blade and ζ is the vortex age relative to the blade azimuth that the vortex originated. The left-hand side (LHS) of Eq. 2 is a one-dimensional wave (convection) equation, with a temporal direction ψ and a spatial direction ζ . The source term on the right-hand side (RHS) of Eq. 2 is non-linear because of the self and mutually induced velocities from the vortices.

The discretized rotor wake problem consists of dividing the vortex filaments along their length into a number of straight-line elementary vortex segments, and applying the governing equation at each collocation point on these vortex segments. These equations are then solved numerically by approximating the partial derivatives on the LHS of Eq. 2 with finite difference approximations. The velocity source term on the RHS of Eq. 2 is evaluated by applying the Biot-Savart law (Ref. 27) to each individual vortex segment and numerically integrating the induced velocities over the length of all vortex filaments.

The free-vortex wake results presented here are calculated using a development of the free-wake analysis of Bagai & Leishman (Refs. 23–26). The original analysis used a second-order accurate pseudo-implicit predictor-corrector (PIPC) relaxation formulation to solve for steady-state (periodic) wake geometry solutions. A five-point central difference scheme is used to approximate the LHS of the governing equations (Eq. 2), while the induced

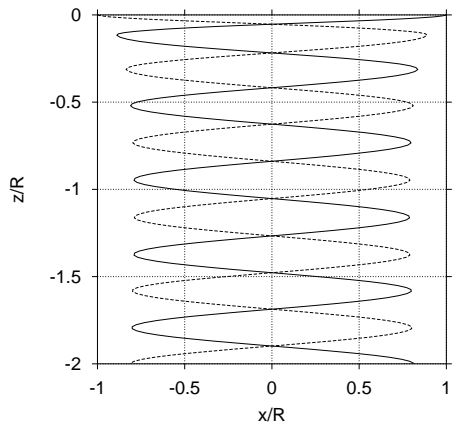
velocities are evaluated using standard straight-line segmentation of the vortices. This five-point scheme has the special property that for equal discretizations along ψ and ζ , the truncation errors from the LHS of the discretized equations cancel each other resulting in an ‘exact’ representation.

The relaxation approach solves for an equilibrium solution by imposing periodicity conditions. In the present work, these equilibrium solutions were used primarily for wake stability analyses, and also as an initial condition for the two newly developed time-marching algorithms (see Appendix). These time-marching algorithms are also second-order accurate predictor-corrector formulations, and allow transient wake geometry calculations with no pre-assumed wake periodicity requirements. The first time-marching algorithm, which is referred to as PCC, uses a five-point central differencing scheme similar to that used in the PIPC relaxation algorithm. The second algorithm, referred to as PC2B, also uses a central difference scheme for the spatial (ζ) derivatives but a second-order backward difference scheme for the temporal (ψ) derivatives. Such a difference scheme introduces additional truncation errors which are both dissipative and dispersive. However, these errors are of a higher order, and the overall solution accuracy is still second-order.

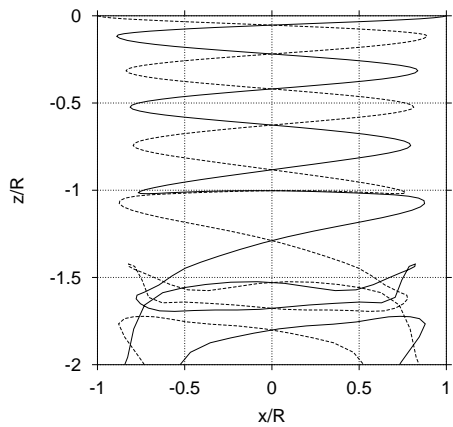
Representative examples of the predicted wake geometries for a two-bladed hovering rotor as obtained using these three free-vortex wake algorithms are shown in Fig. 1; the results being shown for a reference blade azimuth of $\psi_b = 0^\circ$. The rotor was operated at a thrust coefficient of $C_T = 0.005$, with a tip speed of $\Omega R = 89 \text{ ms}^{-1}$. The rotor geometry and operating conditions for this two-bladed rotor are described in Ref. 7. For these calculations, four free-wake turns ($\zeta_{\max} = 1440^\circ$) were used at a discretization of $\Delta\psi = \Delta\zeta = 10^\circ$.

The axisymmetric, periodic and smoothly contracting nature of the relaxation solution shown in Fig. 1(a), is typical of the wake generated by hovering rotors. The two tip vortices followed the same trajectories relative to the blades and were found free from any local or global instabilities. This periodic solution for the wake was used as an initial condition for the two time-accurate algorithms. The calculations were continued in a time-accurate manner for up to fifteen rotor revolutions to allow any initial transient behavior to settle down to equilibrium. The time-accurate solution obtained using PCC algorithm, shown in Fig. 1(b), produced some apparently erratic distortions after about two rotor revolutions. Prior to this, the wake geometry was almost identical to the relaxation solution. The solution obtained using PC2B algorithm, however, was found to be essentially identical to the relaxation solution, as shown in Fig. 1(c).

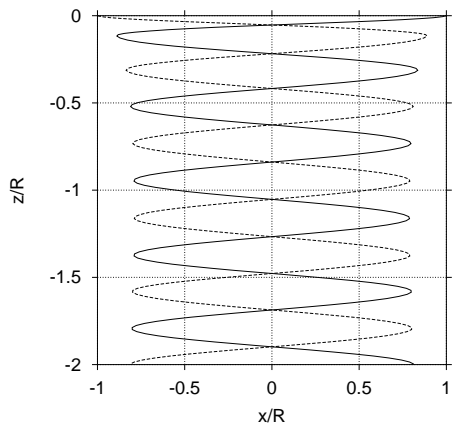
The wake convergence histories corresponding to these three algorithms are shown in Fig. 2 in terms of a RMS



(a) Relaxation (PIPC)



(b) Time-marching (PCC)



(c) Time-marching (PC2B)

Figure 1: Representative free-vortex wake geometries for a two-bladed hovering rotor. The tip vortex from blade 1 (the reference blade) is shown with a solid line, while the tip vortex from blade 2 is shown with a dashed line, $C_T = 0.005$

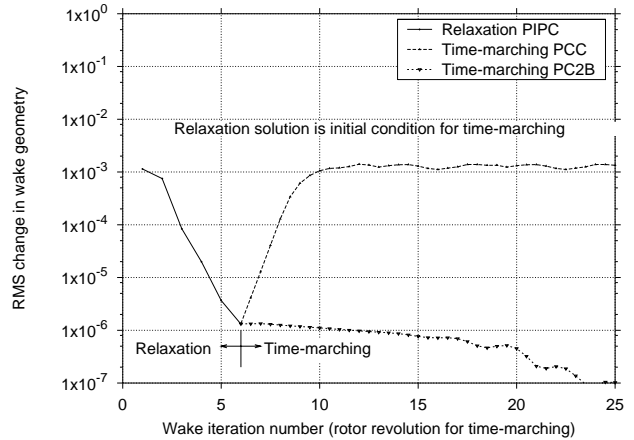


Figure 2: Convergence histories for the free-vortex wake solutions shown in Fig. 1

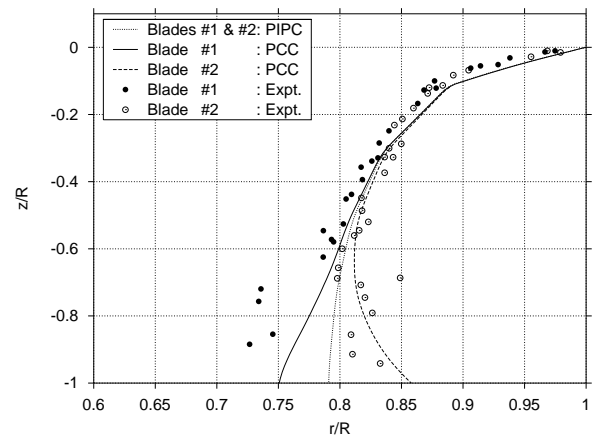


Figure 3: Predicted and measured vortex trajectories in hover as observed in a fixed radial-axial plane, $C_T = 0.005$

change in wake geometry per rotor revolution. The PIPC relaxation solution showed a rapidly converging trend by virtue of wake periodicity enforcement. Starting from such a converged relaxation solution, the PCC time-marching algorithm shows an increased change in wake geometry. Thereafter, the wake geometry continued to change from one rotor revolution to another. This implies that the wake geometry is not periodic at the rotor frequency. However, the change in wake geometry remains bounded and the solution is not divergent. Therefore, the apparently erratic wake distortions seen in Fig. 1(b) are, in reality, deterministic and bounded. Results obtained with the the PC2B time-marching solution, however, showed a continuously converging trend starting from the same initial wake geometry. Any change in wake geometry diminished with time, suggesting that the relaxation solution is, indeed, a steady-state equilibrium solution.

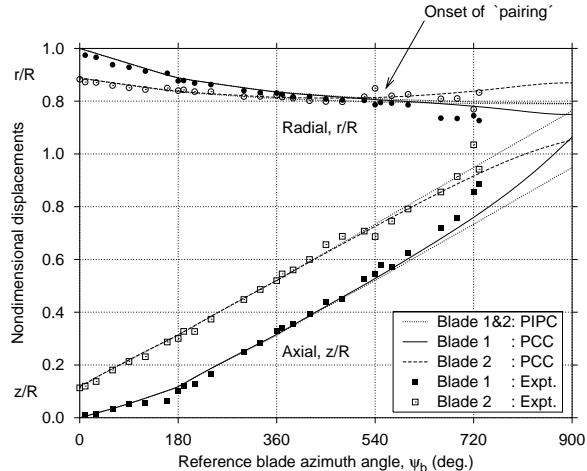


Figure 4: Predicted and measured tip vortex displacements as a function of reference blade azimuthal location, $C_T = 0.005$

Figure 3 shows an alternative presentation where the predicted trajectories of the tip vortices along with the experimental results, as seen from a fixed radial-axial plane. At early vortex ages near the tip path plane (TPP), the tip vortices from the two blades were seen to follow the same trajectory. At later vortex ages, however, these vortices followed different trajectories with one vortex moving radially inward while the other moving radially outward. The azimuth where the two tip vortices cross in the radial direction is the onset of pairing. The PIPC algorithm predicts an axisymmetric wake structure with identical vortex trajectories, and it is the time-accurate PCC algorithm that shows the better agreement with experimental results.

This interesting wake behavior is further elucidated in Fig. 4 by plotting the predicted results in the form of axial and radial tip vortex displacements as a function of the reference blade (blade 1) azimuthal location. The measured vortex trajectories from the experiment reported in Ref. 7 are also plotted for comparison. In this experiment, evidence of vortex pairing was found between tip vortex filaments that were about two rotor revolutions old downstream of the rotor. This pairing phenomenon is evident from the results shown in Fig. 4, which indicate that the trajectories of the two tip vortices cross each other. As noted previously, the relaxation (PIPC) solution is axisymmetric and both tip vortex filaments follow the same trajectory. However, when using the time-accurate solution with the PCC algorithm, the wake was not axisymmetric and the two tip vortex filaments followed different trajectories. In particular, the two vortices formed an interacting vortex pair at an azimuth where the two axial displacement trajectories intersected each other. These

computed results show good agreement with measured trajectories at early vortex ages. The azimuthal location where the two vortices pair, however, is somewhat over-predicted.

To better understand the onset of vortex pairing, a sequence of predicted wake structure for different blade positions (reference blade azimuthal locations) is shown in Figs. 5(a)–(f). The equilibrium (periodic) wake boundary is shown in dotted line. The symbols in Fig. 5(a)–(f) show the vortex trajectories as seen in a fixed radial-axial plane at different times (reference blade azimuth). Note that the vortex filament trailed from blade 1 moves radially inward and axially downward, while that trailed from the blade 2 moves radially outward and axially upward. At a blade azimuth of about 880° one filament loop can be seen to pass through the other. At this azimuth, the two vortices become nearly parallel to the rotor plane forming a vortex pair. This corresponds to the reference blade azimuth shown in Fig. 4, where the axial displacements of two vortex filaments are equal.

Although, there is good agreement between predictions and observations of the vortex pairing phenomenon, the physical mechanism of these interactions occur is not yet clear. For example, it is not immediately obvious as to why the PIPC relaxation algorithm and time-accurate PC2B algorithm fail to predict these vortex interactions despite using identical blade and wake models. The wake vortex trajectories close to the rotor are identical in all three solutions – see Figs. 3 & 4. Therefore, it is expected that vortex interactions originate away from the rotor and would likely have only a small influence on the inflow and blade loads. The mechanism proposed by Tangler *et al.* (Ref. 3) based on experimental observations also suggests that these interactions originate downstream of the region where the full radial contraction of the wake is first obtained, i.e., after about one rotor revolution. The motivation for the following stability analysis is to better understand the physics of this vortex pairing phenomenon.

Linearized Stability Analysis

The rotor wake behavior is now examined by means of a stability analysis, following the methodology applied to linearized flow stability analyses. The rotor wake geometry, as given by a solution to Eq. 1, is the basic equilibrium solution. This equilibrium solution is perturbed by a small quantity, $\delta\vec{r}$, the new geometry being described by $\vec{r} + \delta\vec{r}$. The governing equation for this perturbed wake geometry is

$$\frac{d(\vec{r} + \delta\vec{r})}{dt} = \vec{V}(\vec{r} + \delta\vec{r}) \quad (3)$$

The perturbation equation is the equation governing the perturbation wake displacement, $\delta\vec{r}$, and is obtained by

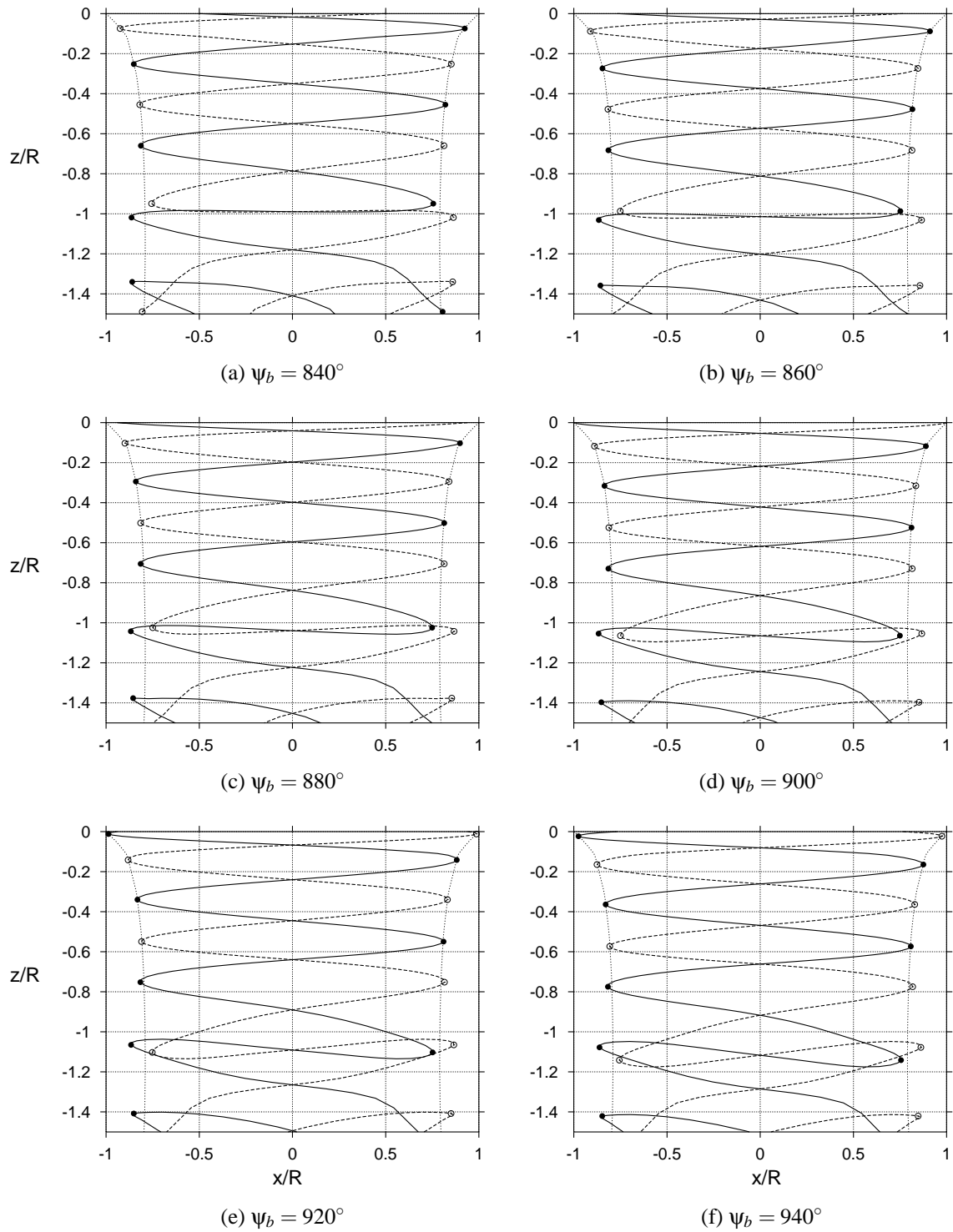


Figure 5: Geometry of two vortex filaments during vortex pairing as predicted using the PCC algorithm for a two-bladed rotor in hover, $C_T = 0.005$

subtracting the equilibrium equation (Eq. 1) from the perturbed equation (Eq. 3), i.e.,

$$\frac{d(\delta\vec{r})}{dt} = \vec{V}(\vec{r} + \delta\vec{r}) - \vec{V}(\vec{r}) \quad (4)$$

The induced velocity on the RHS of Eq. 3 can be expressed as a series in $\delta\vec{r}$, i.e.,

$$\vec{V}(\vec{r} + \delta\vec{r}) = \vec{V}(\vec{r}) + \delta\vec{V}(\delta\vec{r}) + O(\delta\vec{r}^2)$$

The perturbation equation can now be linearized by neglecting higher-order terms in the perturbation $\delta\vec{r}$ to give

$$\frac{d(\delta\vec{r})}{dt} = \delta\vec{V}(\delta\vec{r}) \quad (5)$$

Induced Velocity Perturbation

The induced velocity, $\vec{V}(\vec{r})$, can be obtained by dividing each curvilinear vortex filament into a number of elementary vortex segments, and numerically integrating the induced velocities over the entire filament length. This is most easily accomplished using straight-line segments, which are readily amenable to analytic forms of Biot-Savart law integration. The total induced velocity at a point is then obtained by summation of the velocity induced by each vortex segment. The velocity induced by a vortex element \vec{l} at a point \vec{r} is given by the Biot-Savart (Ref. 27) law as

$$\vec{V} = \frac{\Gamma}{4\pi} \int_l \frac{d\vec{l} \times \vec{r}}{|\vec{r}|^3} \quad (6)$$

Therefore, the velocity induced by a single, straight line vortex element extending from A to B , at a point P (see Fig. 6) can be expressed in the form

$$\begin{Bmatrix} V_x \\ V_y \\ V_z \end{Bmatrix} = \frac{\Gamma_v}{4\pi h} (\cos\theta_1 - \cos\theta_2) \begin{Bmatrix} e_x \\ e_y \\ e_z \end{Bmatrix} \quad (7)$$

where Γ_v is the circulation strength of the vortex element, and where $\vec{r}_1 = \vec{r}_P - \vec{r}_A$, $\vec{r}_2 = \vec{r}_P - \vec{r}_B$, $\vec{l}_{12} = \vec{r}_B - \vec{r}_A$ and $\vec{e} = \frac{\vec{l}_{12} \times \vec{r}_1}{|\vec{l}_{12} \times \vec{r}_1|}$ with $\vec{r}_A, \vec{r}_B, \vec{r}_P$ being the position vectors of

points A , B , and P respectively. Note that this velocity field corresponds to that of a potential vortex, so must exhibit a singularity as $h \rightarrow 0$. Physically, the vortex has a viscous core where the induced velocity resembles solid body rotation. The above equation can be modified to include a viscous vortex core with a core radius of r_c . While various options are possible, in the present work this is done using a general desingularized induced velocity profile with the algebraic form

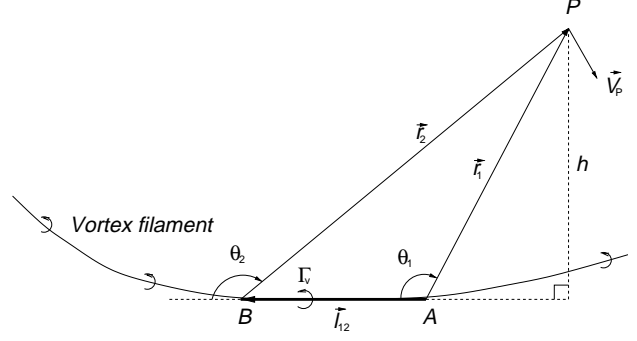


Figure 6: Schematic showing the velocity induced by a straight-line vortex element

$$V = \left(\frac{\Gamma}{2\pi} \right) \frac{r}{(r_c^{2n} + r^{2n})^{1/n}} \quad (8)$$

Note that in the case where $n \rightarrow 0$ the Rankine velocity model is obtained, for $n = 1$ this corresponds to the well-used ‘Scully’ model (Ref. 14), and for $n = 2$ the induced velocity is almost identical in result to that of the Lamb-Oseen model (Ref. 28).

With a desingularized vortex model the above equation for the induced velocity (Eq. 7) is modified into the form

$$\vec{V} = \frac{\Gamma_v}{4\pi} \frac{h}{(r_c^{2n} + h^{2n})^{1/n}} (\cos\theta_1 - \cos\theta_2) \vec{e} \quad (9)$$

Denoting the perturbed quantities by a prime, the perturbed position vectors of the points A , B and P are given by $\vec{r}'_P = \vec{r}_P + \delta\vec{r}_P$, $\vec{r}'_A = \vec{r}_A + \delta\vec{r}_A$, $\vec{r}'_B = \vec{r}_B + \delta\vec{r}_B$. The expression for the induced velocity (Eq. 9) is rewritten in terms of the perturbed quantities, e.g.,

$$h' = h + \delta h, \quad \text{and} \quad \cos(\theta_1)' = \cos(\theta_1) + \delta\cos(\theta_1)$$

The perturbed induced velocity is evaluated up to first-order by neglecting higher-order terms in the perturbations, i.e.,

$$\begin{aligned} \vec{V}' &= \frac{\Gamma_v}{4\pi} \frac{h}{(r_c^{2n} + h^{2n})^{1/n}} \times \\ &\left[h(\cos\theta_1 - \cos\theta_2) \vec{e} \right. \\ &+ h_f \delta h (\cos\theta_1 - \cos\theta_2) \vec{e} \\ &+ h(\cos\theta_1 - \cos\theta_2) \delta \vec{e} \\ &\left. + h(\delta(\cos\theta_1) - \delta(\cos\theta_2)) \vec{e} \right] \quad (10) \end{aligned}$$

The factor, h_f , is a multiplicand of the δh term because of the desingularized viscous velocity profile, and is given by

$$h_f = 1 - \frac{nh^{2n}}{(r_c^{2n} + h^{2n})^{1/n}} \quad (11)$$

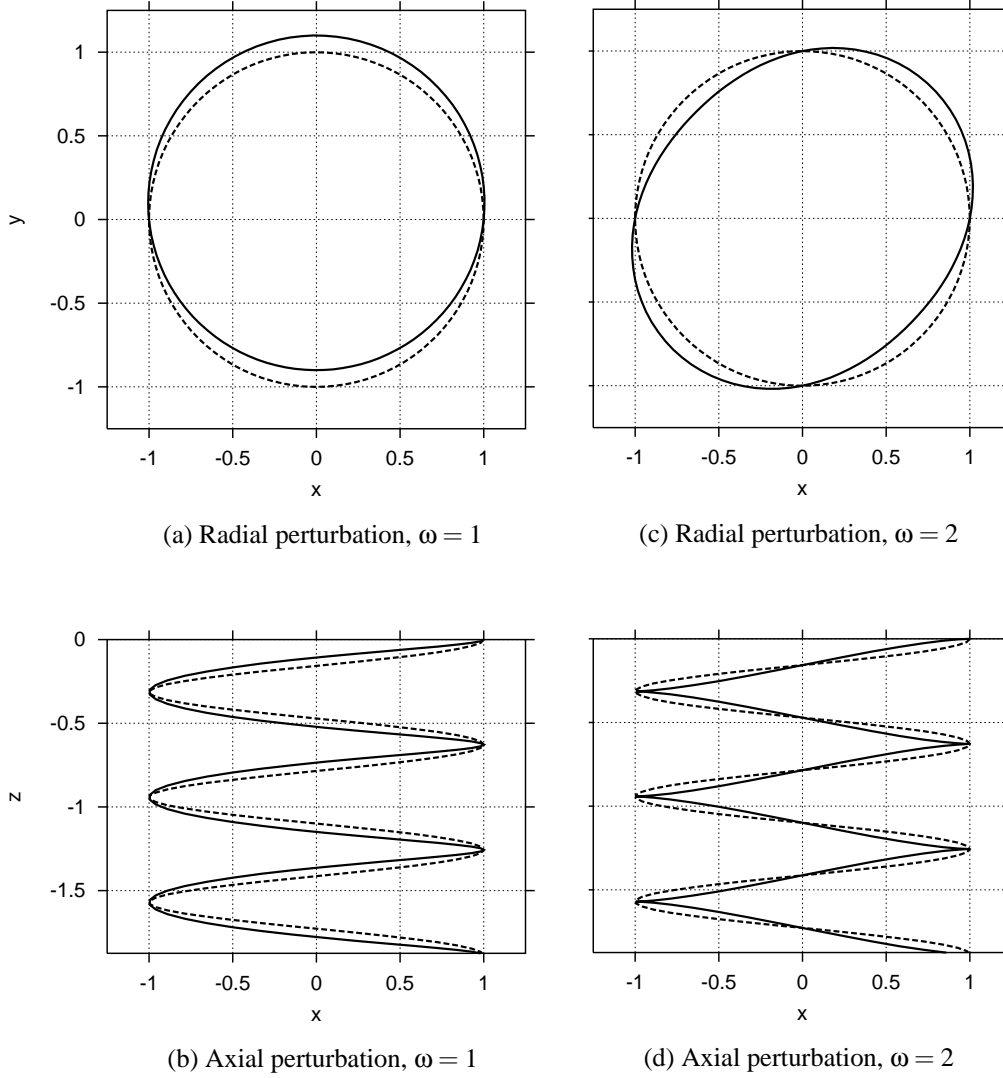


Figure 7: Examples of normal mode perturbations on a helical vortex filament

Each of the perturbation quantities on the RHS of Eq. 10, viz., δh , $\delta(\cos\theta_1)$, $\delta(\cos\theta_2)$, δe_x , δe_y and δe_z , are evaluated up to the first-order by neglecting the higher-order perturbation terms. This can be written in matrix form as, e.g.,

$$\delta h = \{H_A\}^T \{\delta \vec{r}_A\} + \{H_B\}^T \{\delta \vec{r}_B\} + \{H_P\}^T \{\delta \vec{r}_P\} \quad (12)$$

Similarly,

$$\delta(\cos\theta_1) - \delta(\cos\theta_2) = \{C_A\}^T \{\delta \vec{r}_A\} + \{C_B\}^T \{\delta \vec{r}_B\} + \{C_P\}^T \{\delta \vec{r}_P\} \quad (13)$$

and

$$\{\delta \vec{e}\} = [E_A] \{\delta \vec{r}_A\} + [E_B] \{\delta \vec{r}_B\} + [E_P] \{\delta \vec{r}_P\} \quad (14)$$

By assembling these individual matrices, the perturbation induced velocity can be written in the form

$$\{\delta \vec{V}\} = \frac{\Gamma_v}{4\pi} \frac{h}{(h^{2n} + r_c^{2n})^{1/n}} \times \left[[A] \{\delta \vec{r}_A\} + [B] \{\delta \vec{r}_B\} + [P] \{\delta \vec{r}_P\} \right] \quad (15)$$

Normal Mode Perturbation

To simplify the perturbation equations for a stability analysis, the perturbations are assumed to be in the form of a normal mode or a traveling wave.* Because of the heli-

*Any arbitrary disturbance can be transformed into a series of normal mode perturbations, and so the present analysis remains general even after this simplification.

cal nature of the rotor wake, cylindrical polar coordinates are used. These coordinates are also more suitable for understanding the physical nature of the perturbation. The perturbation in cylindrical coordinates is given by

$$\{\delta\vec{p}\} = \begin{Bmatrix} \delta r_0 \\ \delta\theta_0 \\ \delta z_0 \end{Bmatrix} e^{\alpha t + i\omega\zeta} \quad (16)$$

where α is the growth rate and ω is the wave number, that is the perturbation wave has ω cycles for each rotor revolution. An example is shown in Fig. 7 for the radial and axial modes corresponding to $\omega = 1$ and $\omega = 2$. In this case, the equilibrium geometry is a constant pitch, constant radius helix, as shown by the dashed lines, and the perturbed geometry is shown by the solid lines.

The perturbation induced velocities, as derived in the previous section, are evaluated in the Cartesian coordinate system, $\vec{r} = \{x, y, z\}^T$. Therefore, coordinate transformation matrices need to be defined that relate the cylindrical polar coordinates, $\vec{p} = \{r, \theta, z\}^T$, to the Cartesian coordinates. The displacements and perturbations are related by

$$\begin{aligned} x &= r \cos \theta & \delta x &= \delta r \cos \theta - r \sin \theta \delta \theta \\ y &= r \sin \theta & \delta y &= \delta r \sin \theta + r \cos \theta \delta \theta \\ z &= z & \delta z &= \delta z \end{aligned} \quad (17)$$

In matrix form,

$$\begin{Bmatrix} \delta x \\ \delta y \\ \delta z \end{Bmatrix} = [T] \begin{Bmatrix} \delta r \\ \delta \theta \\ \delta z \end{Bmatrix} \quad (18)$$

$$\text{where } [T] = \begin{bmatrix} \cos \theta & -r \sin \theta & 0 \\ \sin \theta & r \cos \theta & 0 \\ 0 & 0 & 1 \end{bmatrix}$$

Also, the velocities and perturbation velocities are given by

$$\{\dot{\vec{r}}\} = [T] \{\dot{\vec{p}}\} \quad (19)$$

$$\{\delta\dot{\vec{r}}\} = [T] \{\delta\dot{\vec{p}}\} + [T_2] \{\delta\vec{p}\} \quad (20)$$

where the second transformation matrix $[T_2]$ is given by

$$[T_2] = \begin{bmatrix} -\dot{\theta} \sin \theta & -\dot{y} & 0 \\ \dot{\theta} \cos \theta & \dot{x} & 0 \\ 0 & 0 & 0 \end{bmatrix} \quad (21)$$

Eigenvalue Problem

The governing equations for each perturbation mode (Eq. 5) can now be solved at a given point P on the vortex filament. The LHS is given by

$$\begin{aligned} LHS = \{\delta\dot{\vec{r}}\} &= [T]_P \{\delta\dot{\vec{p}}\} + [T_2]_P \{\delta\vec{p}\} \\ &= \left[\alpha [T]_P + [T_2]_P \right] \{\delta\vec{p}\} \end{aligned} \quad (22)$$

The subscript denotes that the transformation matrices are evaluated at the point P . The perturbation position vector of point P in Cartesian coordinates is given by

$$\{\delta\vec{r}_P\} = [T] \{\delta_0\} e^{\alpha t + i\omega\zeta_P} \quad (23)$$

The induced velocity perturbation at point P resulting from the i^{th} vortex element, extending from point A to point B , is written in the form

$$\begin{aligned} [\delta V_i] &= [A][T] \{\delta_0\} e^{\alpha t + i\omega\zeta_A} + [B][T] \{\delta_0\} e^{\alpha t + i\omega\zeta_B} \\ &+ [P][T] \{\delta_0\} e^{\alpha t + i\omega\zeta_P} \end{aligned} \quad (24)$$

Considering only the real part, this equation is simplified as

$$[\delta V_i] = [V_i][T] \{\delta\vec{p}\} \quad (25)$$

The velocity contributions of all the vortex elements are summed to obtain the total induced velocity perturbation in the matrix form as $[V] = \sum_i [V_i]$. Therefore,

$$\left[\alpha [T] + [T_2] \right] \{\delta\vec{p}\}_P = [[V][T]] \{\delta\vec{p}\}_P \quad (26)$$

Finally, this equation can be reduced to the standard eigenvalue form

$$\alpha_P \{x\} = [M]_P \{x\} \quad (27)$$

where

$$[M]_P = \left[[V] - [T_2][T]^{-1} \right]_P$$

The eigenvalues α_P give the growth rate of the perturbation at point P on the rotor wake. A positive growth corresponds to an unstable mode, a zero growth rate is a neutrally stable mode, and a negative growth rate is a stable mode.

Results & Discussion

Eigenvalue Analysis

Stability results were obtained from the equilibrium wake geometry and vortex strengths predicted using the free-vortex wake scheme based on the relaxation (PIPC) algorithm. Numerical solutions are chosen mainly because they offer the freedom to study the sensitivity of the results to various rotor geometric and operating parameters, such as number of blades and rotor thrust. However, the eigenvalue analysis developed in the preceding section is completely general, so it can also be applied to any wake geometry including those obtained directly from experimental measurements.

Two different teetering rotor geometries are studied in the present work. In both cases the rotor blades were untwisted with a rectangular planform. Rotor 1 corresponds

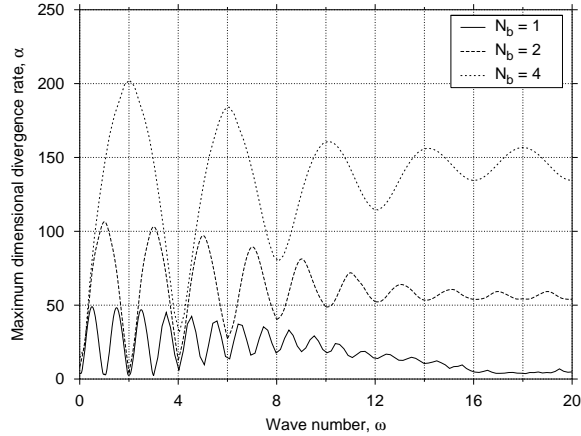


Figure 8: Maximum dimensional divergence rates for the one-, two-, and four-bladed hovering rotors operating at constant blade loading, $C_T/\sigma = 0.0751$

Table 1: Rotor configurations

Configuration	Rotor 1 (Ref. 7)	Rotor 2 (Refs. 8, 9)
Rotor radius, (m)	0.4064	1.0414
Blade chord, (m)	0.0425	0.0762
Tip speed, (ms^{-1})	89.3	196.3

to the configuration described in Ref. 7, while Rotor 2 corresponds to that described in Refs. 8 and 9; the geometric parameters for these two configurations are summarized in Table 1.

Figures 9 and 8 show the maximum predicted divergence rate of the rotor wake as a function of increasing wave number for one-, two-, and four-bladed rotors operating in hover. These rotors were generally similar to Rotor 1 operating at a rotational frequency of 35 Hz and a blade loading of $C_T/\sigma = 0.075$, i.e., at $C_T = 0.0025, 0.005, 0.010$ respectively. The divergence rate, α , is plotted in Fig. 8, and also in a non-dimensionalized form as $\bar{\alpha} = \alpha / \left(\frac{\Gamma}{4\pi R^2} \right)$ in Fig. 9. It is significant to note that the hovering rotor wake is unstable for all operating thrusts, with the divergence rates showing a sinusoidal type of variation for increasing wave number.

In particular, note that the divergence rates increase with increasing number of blades. For rotors operating with the same blade loading (C_T/σ), the one-bladed rotor showed the smallest divergence rates for any given wave number. The dimensional divergence rates (Fig. 8) are also found to be corresponding smaller. The behavior at larger wave numbers indicates the response to high frequency disturbances. The increasing growth rates for

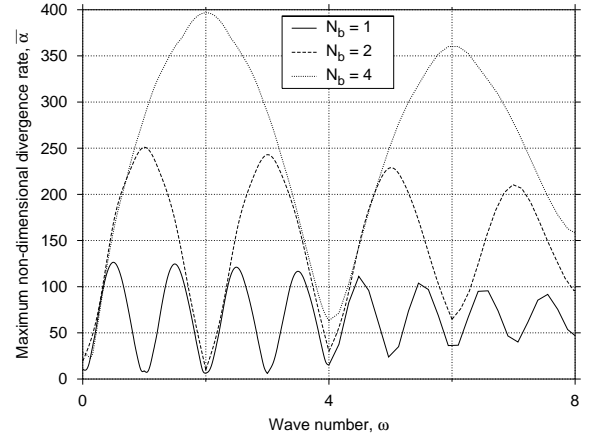


Figure 9: Maximum non-dimensional divergence rates for one-, two-, and four-bladed hovering rotors operating at constant blade loading, $C_T/\sigma = 0.0751$

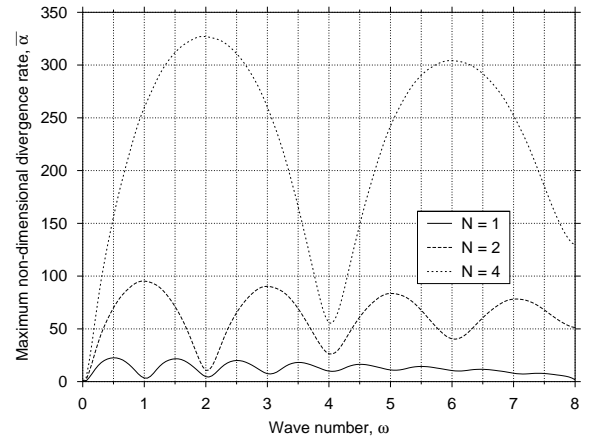


Figure 10: Maximum non-dimensional divergence rates for one, two, and four intertwining helical vortex filaments

large wave numbers with increasing number of blades suggest increased susceptibility to instabilities from random disturbances, e.g., external turbulence or recirculation in the test facility. This is consistent with the experimental observation that the aperiodicity of a rotor wake has a tendency to increase with increasing number of blades (Ref. 11).

The wave numbers corresponding to the extrema in the divergence rates closely correlate with the number of rotor blades. It can be seen that a maximum divergence rate occurs at wave numbers equal to half-integer multiples of the number of blades, i.e., at wave numbers $\omega = \left(k + \frac{1}{2}\right) N_b$, for all integer k . On the other hand, a minimum divergence rate occurs at integer multiple of the number of blades, that is $\omega = k N_b$. With increasing wave number, the peak-to-peak amplitude decreases (i.e., the difference between

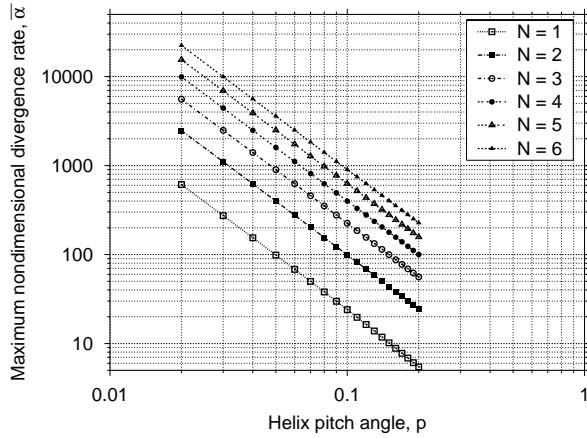


Figure 11: Absolute maximum non-dimensional divergence rate for intertwining infinite helical vortex filaments

maximum and minimum divergence rates decreases), indicating that for very large wave numbers the divergence rate would be independent of the wave number, as shown in Fig. 8. A similar trend was reported in Ref. 6 for the predicted stability of interdigitated infinite helical vortices. Even though an infinite helix is not an accurate representation of a helicopter rotor tip vortex filament, a stability analysis of helical vortices will give a qualitatively accurate estimation of the stability characteristics of the rotor wake.

Helical Vortex Filaments

To bring out the close resemblance between the stability of helical vortices and a rotor wake, non-dimensional growth rates for helical filaments are presented in Fig. 10. Infinite helical vortex filaments were approximated by considering ten turns above and below the part of the filament being examined. The striking similarity between the stability characteristics of these helical vortices and the rotor wake (see Fig. 9) is evident from the sinusoidal behavior with respect to wave number. The growth rates also increased with increasing number of intertwining filaments, similar to increasing number of blades. Growth rates reported by Gupta & Loewy in Ref. 6 showed a quadratically decreasing trend with increasing helical pitch, p . Similar results are shown in Fig. 11 where the quadratic decreasing trend is seen clearly from the slope of the log-arithmetic plot. The divergence rate also increased with increasing number of helical filaments, as reported in Ref. 6.

Figure 12 shows the same results plotted as a function of the distance between two adjacent vortex filaments ($= 2\pi p/N$). The results for different number of helical filaments were found to coalesce onto a single curve, indicating that the predominant factor affecting the divergence

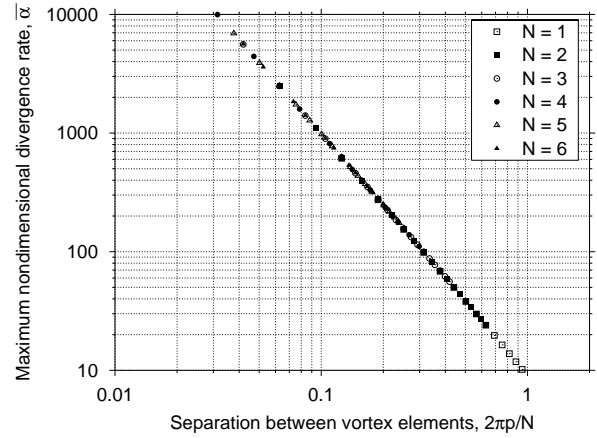


Figure 12: Absolute maximum non-dimensional divergence rate for infinite helical vortex filaments as a function of separation between adjacent vortex segments

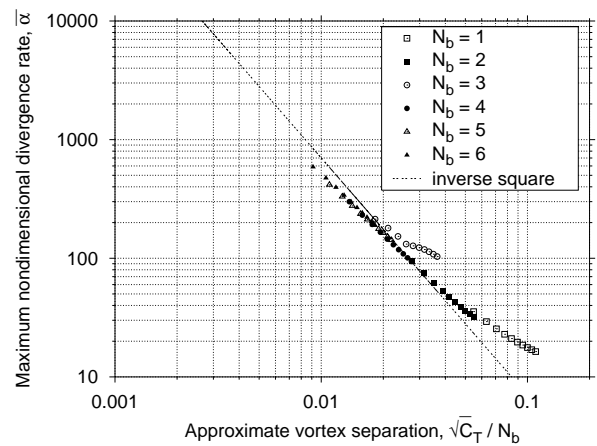


Figure 13: Absolute maximum non-dimensional divergence rate for hovering rotor wake a function of (approximate) separation between adjacent vortex segments

rates is the distance between two adjoining vortices. Two interdigitated helical filaments are, indeed, equivalent to a single helical filament with half the pitch, and so forth. This striking result is expected because the divergence rate of a normal mode depends on the vortex induced velocities, which are proportional to the inverse square of distance from the vortex.

Rotor Wake Vortices

The actual hovering rotor wake also shows a similar behavior. The separation distance between two adjacent tip vortex segments is directly proportional to the mean inflow and inversely proportional to the number of blades, i.e., it is proportional to the blade loading. Therefore, the

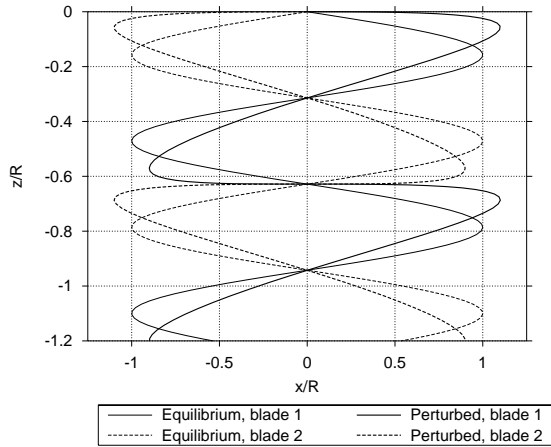


Figure 14: Schematic of $\omega = 1$ deformation mode for a two-bladed hovering rotor

absolute maximum divergence rates are plotted as a function of $\sqrt{C_T}/N_b$ in Fig. 13. The results showed the same nominal trend as suggested by the helical vortex filament results shown previously. The deviations from an inverse square trend are because the actual wake geometry does not have a constant pitch and radius like the idealized helical case. However, the qualitative behavior is remarkably similar.

Vortex Pairing Instability

The most unstable mode for the one-bladed rotor is the $\omega = 1/2$ mode, which corresponds to a sub-harmonic disturbance along the length of the tip vortex trajectory. In practice, it is known from experimental studies that the wake generated by a one-bladed rotor is the most stable to study experimentally. In experimental tests with rotors, the most common physical disturbances affecting the wake originate from supports, an airframe or other nearby structures, or slight mistracking of the blades. These disturbances would provide a source of a once-per-revolution perturbation to the blade(s) and the rotor wake. It will be seen from Figs. 8 and 9 that the divergence rate for the $\omega = 1$ mode is a minimum for the one-bladed rotor. The two-bladed rotor, however, shows a maximum divergence rate corresponding to this wave number, and therefore, this $\omega = 1$ wake deformation mode for two-bladed rotors is the most likely to exhibit an instability.

The $\omega = 1$ unstable deformation mode is schematically shown in Fig. 14 for a two-bladed rotor wake. Both radial and axial perturbations are shown with reference to an equilibrium geometry consisting of two helical vortex filaments with constant pitch and radius. For this mode, the perturbations for the two filaments are 180° out-of-phase

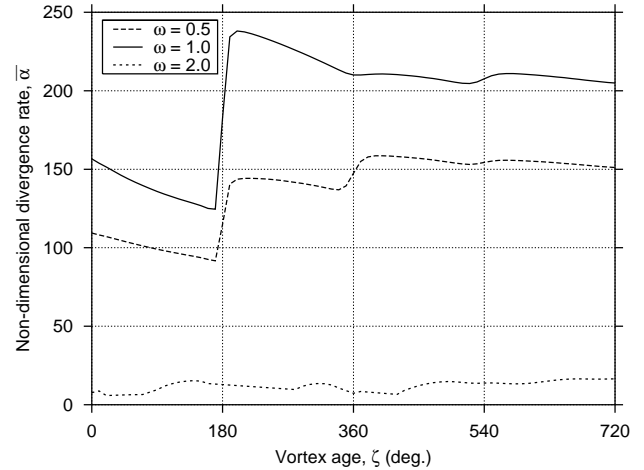


Figure 15: Variation in non-dimensional wake divergence rate with increasing vortex age for Rotor 1 in hover

with respect to each other. The vortex from one blade moves radially inward and axially downward, while the vortex from the other blade moves radially outward and axially upward relative to the respective equilibrium positions. For all perturbation modes with $\omega = (k + \frac{1}{2})N_b$, the vortex filament perturbations are out-of-phase, and a local maximum divergence rate is obtained for these wave numbers. Furthermore, with the $\omega = kN_b$ modes the two filament perturbations are in-phase and a minimum divergence rate is observed. Therefore, stability of the wake geometry is seen to be strongly dependent on the relative phasing of the perturbations of individual vortex filaments. The opposite phasing of the two filaments in Fig. 14 appears in the form of ‘pairing’ of the two vortices. This confirms that the vortex pairing observed on two-bladed rotors is a long-wave instability corresponding to the unstable wake deformation mode with a wave number of $\omega = 1$. Therefore, the vortex pairing phenomenon will most likely be observed in the wake of a two-bladed rotor, which seems to be confirmed in light of recent experimental evidence by Martin *et al.* (Ref. 7) and Caradonna *et al.* (Refs. 8, 9).

It was seen in numerical results that a wake instability was originated at a vortex age of approximately $\zeta = 2\pi/N_b = 180^\circ$. Tangler *et al.* (Ref. 3) have also reported that the vortex pairing instability originated at approximately the same vortex age, where the wake has undergone a maximum radial contraction. To understand this behavior, the divergence rates for Rotor 1 are plotted in Fig. 15 as a function of increasing vortex age for three representative perturbation modes. As previously described, the $\omega = 1$ mode shows the largest divergence rate, with a maximum occurring just after $\zeta = 180^\circ$. The divergence rates show a sharp increase at that vortex age. The $\omega = 0.5$

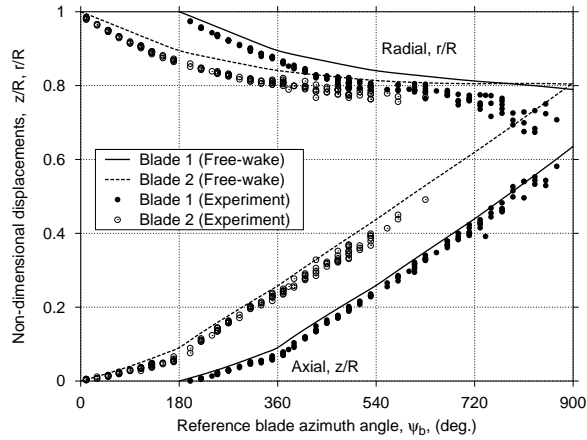


Figure 16: Predicted and measured tip vortex locations for the baseline (tracked) rotor

mode shows a similar qualitative trend but with a smaller magnitude. The $\omega = 2$ mode shows the smallest divergence rate, which is nominally the same for all vortex ages. The low divergence rate at early vortex ages explains the empirical observation that the rotor wake at early vortex ages is mostly free from any instabilities and shows a steady, nearly periodic behavior. The instability appears to originate at approximately the location where the rotor wake has undergone a maximum radial contraction, as hypothesized by Tangler *et al.* (Ref. 3).

Mistracked Rotor

One possible factor initiating a vortex pairing instability is a slight mistracking of the blades. This will result in tip vortices of unequal circulation strength, possibly exciting an unstable deformation mode. Tangler *et al.* (Ref. 3) postulated such mistracking to be the cause of asymmetry of hovering wake, and also the vortex pairing instability. As an extension of the work of Martin *et al.* (Ref. 7), a laser light sheet flow visualization experiment has been conducted with a deliberately mistracked two-bladed rotor to explore the effects on wake stability. The rotor geometry and operating conditions were same as Rotor 1, with one blade set at 1° lower pitch angle. The results are shown in Figs. 16 and 17. For the baseline (tracked) rotor, the vortices did not exhibit pairing up to a vortex age of about 900° , as shown in Fig. 16. However, for the mistracked rotor, the vortices formed a pair at a blade azimuth of approximately 540° , which is the azimuth where the two vortex trajectories can be seen to intersect in Fig. 17. In both cases, the predictions using the free-vortex wake model show good agreement with the experimental results; in particular, the early tip vortex pairing observed with the mistracked rotor is very well predicted.

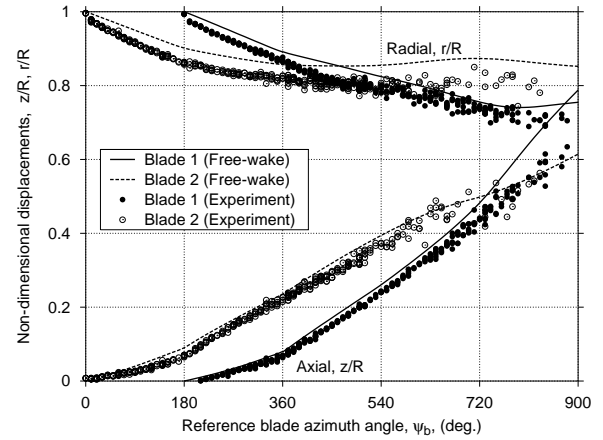


Figure 17: Predicted and measured tip vortex locations for the mistracked rotor

One important difference between the wake geometries of the baseline and tracked rotors is the asymmetry of the rotor wake. The laser light-sheet flow visualization does not bring out this asymmetry because the measured tip vortex locations can only be obtained up to a vortex age of about 900° . The schlieren results in Ref. 3 show that the wake is symmetric for about two rotor revolutions below the rotor, while the far-wake is highly asymmetric. The numerical results predict a distinctive asymmetry for both equilibrium and unsteady (transient) wake solutions.

This asymmetry is evident when the results shown above are plotted again in the form of tip vortex trajectories in a fixed $r-z$ plane. The baseline results in Fig. 18 showed that the two vortices followed almost identical trajectories near the rotor plane. However, further downstream from the rotor the two tip vortices followed different trajectories showing evidence of vortex pairing. This was observed during the wake visualization experiments, however, the increased aperiodicity of the wake in this region did not allow accurate measurements of the tip vortex displacements.

The predicted wake geometry remains symmetric even in the far wake region, where vortex pairing is evident on both sides of the rotor wake. For the mistracked rotor, the two vortices follow different trajectories much closer to the rotor plane, as shown in Fig. 19. This leads to an earlier onset of the pairing instability, and suggests an increased susceptibility to instabilities. The other important difference is the asymmetry of the trajectories in the far-wake caused by unequal tip vortex strengths. Based on classical vortex dynamics considerations, the asymmetry may be caused by the weaker vortex rotating around the stronger vortex during pairing.

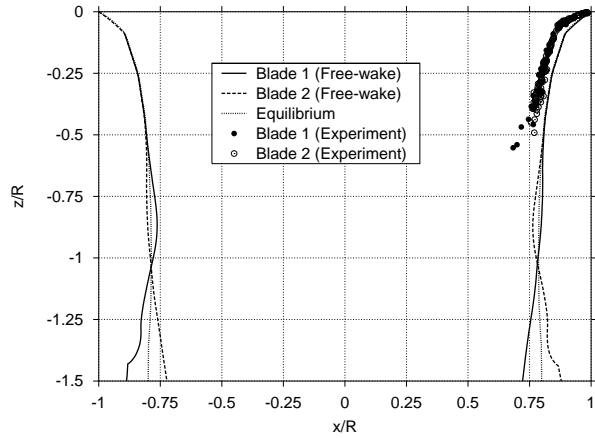


Figure 18: Predicted and measured tip vortex locations for the baseline (tracked) rotor

Effect of Rotor Operating State

Tangler *et al.* (Ref. 3) observed empirically that the vortex pairing occurred further away from the rotor with increasing collective pitch angle, or rotor thrust. A similar observation is reported by Caradonna *et al.* (Refs. 8, 9) with increasing collective pitch as well as with increasing climb rate. Figure 20 shows the effect of increasing rotor thrust on the calculated divergence rate of a hovering rotor wake. These results are calculated for Rotor 2 (Refs. 8, 9). The divergence rate for a given wave number was found to decrease with increasing thrust, that is the wake was less susceptible to instabilities. A less strong instability indicates that any unstable deformation mode will grow more slowly. Therefore, the vortex pairing will be observed at a greater distance downstream from the rotor disk, as has been observed in experiments (Refs. 8, 9). It must be noted that the wake generated by Rotor 2 shows as smaller divergence rate in hover compared to that for Rotor 1, suggesting that the wake geometry is less unstable. This appears to contradict the experimental observations because the rotor wake observed in Refs. 8 and 9 exhibited a strong, repeatable pairing phenomenon. These differences may be because of different sources of disturbances inherent to the two experimental set-ups in Ref. 7 and Refs. 8 & 9.

The wake instability is a result of the vortex induced velocities and, therefore, depends on both the vortex strength and separation distance between two vortex filaments. As rotor thrust increases, both the strengths of the vortices and the axial spacing between two vortex filaments increase. Increased vortex strength implies increased divergence rate, while increased axial spacing between the vortices implies a decreased divergence rate. Note that the velocity induced by one vortex element at another is directly proportional to the vortex strength, but inversely propor-

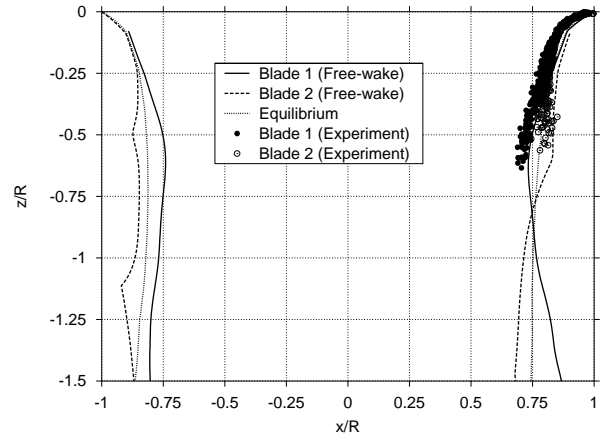


Figure 19: Predicted and measured tip vortex locations for the mistracked rotor

tional to their separation distance. Therefore, the separation distance between adjacent vortices plays a more dominant role than the vortex strength in determining the stability of the rotor wake geometry.

Figure 21 shows the effect of climb rate on the stability of the wake computed at (a) constant rotor thrust of $C_T = 0.004$, and (b) constant collective pitch angle of $\theta_0 = 11^\circ$. The rotor geometry in this case corresponds to Rotor 2. In both cases the divergence rates decrease with increasing climb rate, therefore, vortex pairing would take place further downstream in the wake away from the rotor. This is consistent with the trend reported in Refs. 8 and 9 for a constant collective pitch. In the first case, the tip vortex strengths remain nominally constant, while the axial separation distance between two vortex filaments increases with climb rate. A significant reduction in divergence rate is seen during the transition from hover to a small climb rate, but with successively smaller reductions at higher climb rates. In the second case with constant collective pitch, the rotor thrust and the tip vortex strengths decrease with climb rate, while the axial separation of the vortex filaments increases only relatively slowly. In this case, the wake divergence rates gradually decreased with increasing climb rate. This supports the previous observation that the wake stability is dependent predominantly on the axial separation distance between adjacent vortex filaments.

The vortex pairing phenomenon is, therefore, an inherent rotor wake characteristic and is a naturally unstable deformation mode of rotor wakes in axial flight. This also implies that in the absence of any perturbations the wake geometry remains in its periodic, equilibrium state. However, in experiments various physical disturbances inherent to the experimental set-up may provide the conditions necessary to excite the equilibrium wake geometry and

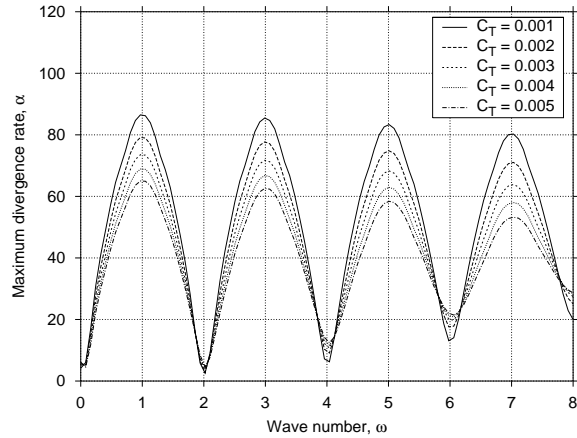


Figure 20: Effect of increasing rotor thrust on the maximum divergence rates of the wake for Rotor 2 in hover

cause it to become unstable. In computational results, it is the numerical truncation and round-off errors that potentially lead to the instability. It is interesting to note that the same unstable mode is excited because of different disturbances.[†] For a two-bladed rotor, the $\omega = 1$ mode is the first unstable perturbation mode, that is the mode corresponding to the smallest wave number and to a maximum divergence rate. This mode is the most predominant in response to small disturbances of different origins.

Free-Vortex Wake Numerical Issues

These empirical wake stability characteristics also give insight into understanding the differences shown between ‘relaxation’ and ‘time-accurate’ free-vortex wake methods, as shown previously in Fig. 1. The results in Fig. 9 show that for $\omega = kN_b$ perturbation modes the wake divergence rates are the smallest; that is, the wake geometry is least unstable. Relaxation based free-wake methods such as the PIPC scheme allow only these $\omega = kN_b$ perturbation modes to arise from numerical errors because periodicity conditions are imposed on the wake geometry. Because these perturbation modes are the least unstable, such numerical errors in the solution do not grow significantly with the number of wake iterations. Therefore, relaxation free-wake solutions usually appear free from any apparent instabilities.

Conversely, transient or time-marching free-wake solutions (which do not enforce periodicity) allow disturbances in the form of all modes. Therefore, the smallest unstable mode is predominantly excited, and these solutions usually show an instability mode closely resembling

[†]This is analogous to the first natural mode of a vibrating beam, which is the predominant response to arbitrary small disturbances.

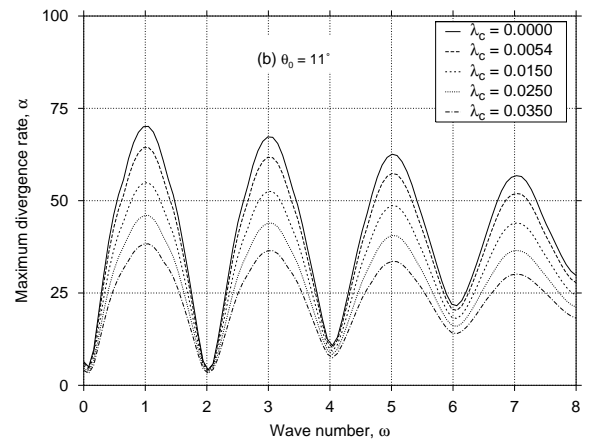
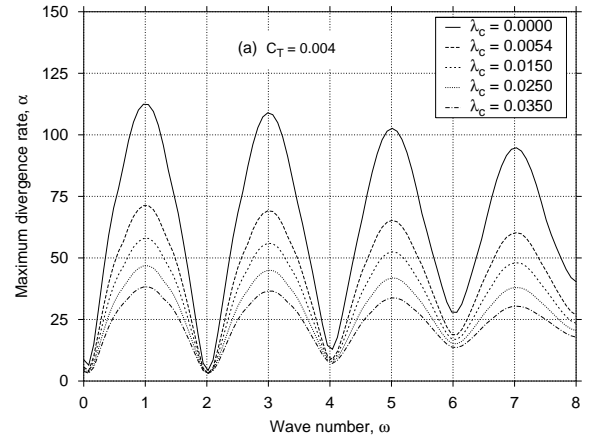


Figure 21: Effect of increasing axial climb rate on maximum wake divergence rates for Rotor 2 with (a) constant thrust, $C_T = 0.004$ (b) constant collective, $\theta_0 = 11^\circ$

the $N_b/2$ wave number. However, note from Fig. 1 that the PC2B algorithm does not exhibit these instabilities. The reason for this behavior lies in the truncation errors in the PC2B difference scheme, which provide a higher numerical viscosity thereby causing the numerical disturbances to dissipate (see Appendix).

Numerical truncation errors in free-vortex wake schemes may provide the perturbations to the equilibrium wake geometry, which will manifest as some form of wake instability. These instabilities, in many cases, may closely mimic the physical instabilities observed in experiments. Many free-vortex wake solutions have been found to exhibit a wake instability in hovering flight, i.e., the wake geometry did not converge to an equilibrium solution (Refs. 13, 18, 22). The instability becomes evident in the form of mutual interaction of vortex filaments, which often results in long-wave disturbances on the vortex filaments, and ultimately in a form of vortex pairing. While similar instabilities have also been ob-

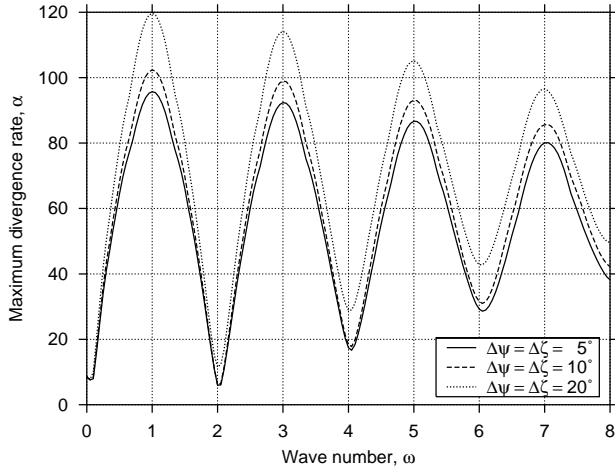


Figure 22: Effect of wake discretization on the stability of a numerical wake solution. Rotor 1 in hover, $C_T = 0.005$

served in sub-scale rotor wake experiments (Refs. 2, 3), these instabilities were generally not as severe as those observed in free-vortex wake analyses (Ref. 29). Subsequent research has demonstrated that many of these numerical instabilities can be overcome through the use of improved numerical methods for solving the wake equations, e.g. semi-implicit (Ref. 20) or pseudo-implicit methods (Refs. 21, 23–26), and influence coefficient based methods (Refs. 18, 22).

In most numerical or computational studies a physical instability refers to the natural, inherent instability of the solution. A numerical instability, typically, refers to a non-physical instability that is not inherent to the solution, but is caused because of the numerical method itself. Because the hovering rotor wake is inherently unstable, any instabilities seen in numerical results are often regarded as physical instabilities. However, this may not always be the case. It is important to remember that the rotor wake is ‘unstable’ implies that it is in ‘unstable equilibrium,’ i.e., the wake structure would remain in this state of unstable equilibrium until it is disturbed because of some external disturbance. An instability is the behavior of the wake caused by such a disturbance to an unstable equilibrium state. Therefore, instabilities observed in experiments imply that the equilibrium wake structure is unstable, and also that external disturbances are present in the flowfield.

Numerical results, such as those presented in the previous sections, show that the numerical solution is unstable, similar to the real wake geometry. However, the numerical solution may not exhibit an instability. This is because no disturbances are being explicitly modeled in the numerical scheme, and in the absence of any such disturbances the wake must remain in a state of unstable equilibrium. Physical instabilities, such as observed in experiments,

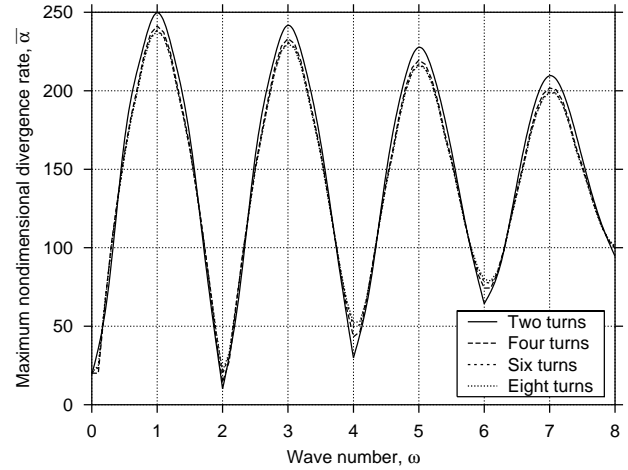


Figure 23: Effect of increasing number of free-wake turns on the stability of the numerical wake solution. Rotor 1 in hover, $C_T = 0.005$

may be obtained in numerical simulations by explicitly modeling disturbances in the flowfield. In the absence of such disturbances being modeled, any instability in the numerical solution is non-physical. Instabilities resulting from disturbances in the form of truncation/round-off errors implicit in the numerical scheme must, therefore, be regarded as a numerical instability. Such numerical errors are almost always present in numerical analyses, and may potentially disturb a solution in unstable equilibrium. Therefore, a proper choice of numerical algorithm is necessary to avoid numerical instabilities.

Because the disturbances leading to the instability observed in the PCC wake solution are of a numerical origin, this numerical instability will be dependent on various numerical parameters such as wake discretization, far-wake truncation, and even the viscous vortex model. Figure 22 shows the influence of wake discretization on the divergence rates of a hovering rotor wake. The wake geometries are obtained for the two-bladed rotor (Rotor 1) using four turns of free-vortex wake. The divergence rates showed a slightly decreasing trend with increased grid resolution (higher fidelity discretization). The rotor operating conditions were identical in all the cases, and therefore, the strength of the tip vortices were nominally constant. The differences in divergence rates must then be a result of different vortex separation distances. This is because of the second-order errors in the induced velocity computations. With improved grid discretization, the induced velocity is computed with smaller errors, and so the tip vortices exhibit slightly different axial displacements. Because the divergence rates (like the induced velocities) are inversely proportional to the separation distance, small variations in vortex separation distance are reflected in the

wake divergence rates.

Another source of potential errors results from the vortex wake truncation at the far-wake boundary, that is, well downstream of the rotor toward infinity. In a practical sense, free-vortex wake calculations must always be performed with a finite number of free wake turns. Because of this finite wake truncation, small errors are introduced in the induced velocity calculation at each collocation point. Although these errors are usually much smaller than the precision required for engineering analysis of rotor performance and blade loads, they may affect the wake stability and may lead to the initiation and growth of an artificial vortex pairing instability. This instability may, in turn, adversely affect blade airloads and rotor performance predictions.

To show this latter effect, the wake geometry was computed using 2, 4, 6 and 8 free-wake turns, and the divergence rates corresponding to these cases is shown in Fig. 23. Note that the divergence rates show some sensitivity with fewer number of free-vortex turns of the wake. However, the discrepancy decreases as the number of turns are increased; the divergence rates for 6 and 8 free turns are almost identical. As the divergence rate decreases, the pairing between individual vortex filaments would occur further downstream in the wake below the rotor.

It can be seen from Figs. 22 and 23, that the numerical errors are minimized by using a finer wake discretization or larger number of free turns, leading to smaller divergence rates. Therefore, the amplitude of the numerical instability will be smaller when the numerical errors are smaller. This will result in a delayed onset of vortex pairing, as shown in Fig. 24. It can be seen that in all cases, the wake instability initiates at about a vortex age of $\zeta = 180^\circ$, where the trajectories of the two vortex filaments separate from each other. The magnitude of the instability grows more slowly with a larger number of free-wake turns, as can be seen from the increasing azimuthal location of vortex pairing, that is, where the two vortex trajectories intersect each other. This is consistent with the smaller wake divergence rate as predicted using the eigenvalue-based stability analysis. Increasing refinement of the discretization also results in a similar trend. These results confirm that this vortex pairing is indeed a numerical manifestation of the wake instability and, therefore, can be modified by controlling the numerical parameters. Because the initial deformation leading to the instability (i.e., a perturbation to an equilibrium wake geometry) will be different in experimental tests and numerical results, an agreement between the two may, in some cases, be entirely fortuitous.

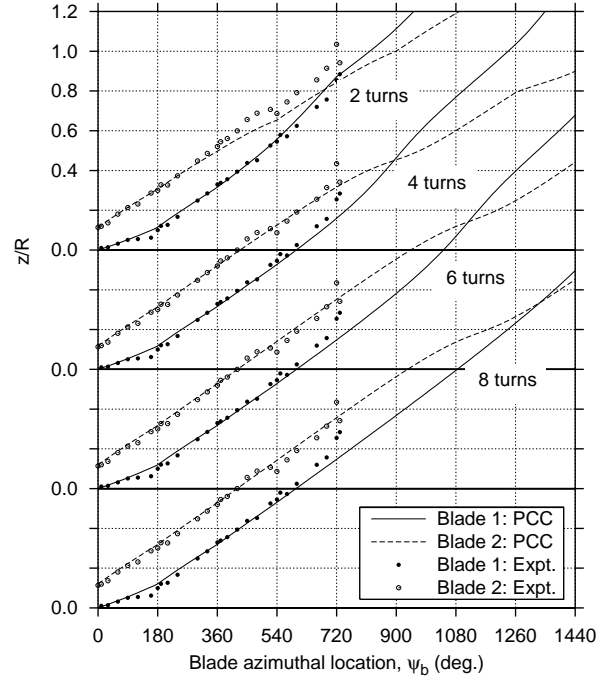


Figure 24: Effect of increasing number of free-wake turns on the numerical wake geometry solution. Rotor 1 in hover, $C_T = 0.005$

Conclusions

An eigenvalue analysis has been developed to study the stability characteristics of helicopter rotor wakes in hover and axial climb. A hovering rotor wake was shown to be unstable for all perturbation modes, but the wake stability improves with increasing rotor thrust or climb velocity. The mutual vortex interactions, such as the tip vortex pairing often observed experimentally, were shown to correspond to a unstable long-wave deformation mode. The specific conclusions drawn from this study are:

1. The wake divergence rate showed a rapid increase at a tip vortex age corresponding to the first blade passage, i.e., $\zeta = 2\pi/N_b$. This suggests that the rotor wake is relatively stable while it is undergoing the initial radial contraction, as confirmed by experiments.
2. The divergence rate for an unstable deformation mode decreases with increasing rotor thrust. The increased tip vortex separation distance (or the helical pitch) has a stronger influence on the wake stability characteristics. Therefore, the divergence rates also showed a decreasing trend with increasing axial climb velocity.

3. The vortex pairing phenomenon, as sometimes noted in rotor experiments and numerical solutions of the rotor wake, is recognized as a long-wave ($\omega = 1$) instability mode of the wake. This instability manifests in experiments because of various inherent physical disturbances. In numerical solutions, these disturbances have their origin in truncation/round-off errors, as shown by its dependence on numerical parameters like discretization level and number of wake turns. Therefore, agreement between experiments and numerical results is not always possible, and many otherwise good correlations may often be fortuitous.
4. The relaxation free-vortex wake algorithms converge to equilibrium (periodic) wake geometries, while time-accurate algorithms, typically, exhibit instabilities. By enforcing periodicity, the relaxation algorithms allow only N_b -per-revolution disturbances. Because these disturbance modes are least unstable, the periodic wake algorithms (like the relaxation methods) are generally not susceptible to wake instabilities. However, by a proper choice of numerical algorithm it is possible to obtain a time-accurate wake solution that is free from any artificial (non-physical) instabilities.

Acknowledgments

This work was supported by the National Rotorcraft Technology Center under grant NCC 2944. The authors would like to thank Preston Martin and Greg Pugliese for making the fascinating flow visualization measurements.

References

- ¹Leishman, J. G., and Bagai, A., "Challenges in Understanding the Vortex Dynamics of Helicopter Rotor Wakes," *AIAA Journal*, Vol. 36, No. 7, July 1998, pp. 1130–1140.
- ²Landgrebe, A. J., "The Wake Geometry of a Hovering Rotor and its Influence on Rotor Performance," *Journal of the American Helicopter Society*, Vol. 17, No. 4, October 1972, pp. 2–15.
- ³Tangler, J. L., Wohlfeld, R. M., and Miley, S. J., "An Experimental Investigation of Vortex Stability, Tip Shapes, Compressibility, and Noise for Hovering Model Rotors," NASA CR-2305, 1973.
- ⁴Levy, H., and Forsdyke, A. G., "The Steady Motion and Stability of a Helical Vortex," *Proceedings of the Royal Society, Series A*, Vol. 120, 1928.
- ⁵Widnall, S. E., "The Stability of a Helical Vortex Filament," *Journal of Fluid Mechanics*, Vol. 54, No. 4, 1972, pp. 641–663.
- ⁶Gupta, B. P., and Loewy, R. G., "Theoretical Analysis of the Aerodynamic Stability of Multiple, Interdigitated Helical Vortices," *AIAA Journal*, Vol. 12, No. 10, October 1974, pp. 1381–1387.
- ⁷Martin, P. B., Bhagwat, M. J., and Leishman, J. G., "Strobed Laser-Sheet Visualization of a Helicopter Rotor Wake," Paper PF118, Proceedings of PSFVIP-2, Honolulu, HI, May 1999 also, *Journal of Flow Visualization & Image Processing* (in press).
- ⁸Caradonna, F., Hendley, E., Silva, M., Huang, S., Komerath, N., Reddy, U., Mahalingam, R., Funk, R., Wong, O., Ames, R., Darden, L., Villareal, L., and Gregory, J., "An Experimental Study of a Rotor in Axial Flight," Proceedings of the AHS Technical Specialists' Meeting for Rotorcraft Acoustics and Aerodynamics, Williamsburg, VA, October 28–30 1997.
- ⁹Caradonna, F., Hendley, E., Silva, M., Huang, S., Komerath, N., Reddy, U., Mahalingam, R., Funk, R., Wong, O., Ames, R., Darden, L., Villareal, L., and Gregory, J., "Performance Measurement and Wake Characteristics of a Model Rotor in Axial Flight," *Journal of the American Helicopter Society*, Vol. 44, No. 2, 1999, pp. 101–108 (Errata, Vol. 44, No. 3).
- ¹⁰Jain, R., Conlisk, A. T., Mahalingam, R., and Komerath, N. M., "Interaction of Tip-Vortices in the Wake of a Two-Bladed Rotor," Proceedings of the 54th Annual American Helicopter Society Forum, Washington, DC, May 1998.
- ¹¹Leishman, J. G., "On the Aperiodicity of Helicopter Rotor Wakes," *Experiments in Fluids*, Vol. 25, 1998, pp. 352–361.
- ¹²Chung, K. H., Na, S. U., Jeon, W. H., and Lee, D. J., "A Study on Rotor Tip-Vortex Roll-Up Phenomenon by Using Time-Marching Free-Wake Method," Proceedings of the 56th Annual American Helicopter Society Forum, Virginia Beach, VA, May 2000.
- ¹³Crimi, P., "Theoretical Prediction of the Flow in the Wake of a Helicopter Rotor," Cornell Aeronautical Laboratory Report BB-1994-5-1, Buffalo NY, September 1965.
- ¹⁴Scully, M. P., "A Method of Computing Helicopter Vortex Wake Distortion," Massachusetts Institute of Technology Report No. ASRL TR 138-1, June 1967.
- ¹⁵Landgrebe, A. J., "An Analytical Method for Predicting Rotor Wake Geometry," Presented at the AIAA/AHS VTOL Research, Design & Operations Meeting, Atlanta, GA, February 1969.

¹⁶Clark, D. R., and Leiper, A. C., “The Free Wake Analysis – A Method for Prediction of Helicopter Rotor Hovering Performance,” *Journal of the American Helicopter Society*, Vol. 15, No. 1, January 1970, pp. 3–11.

¹⁷Egolf, T. A., “Rotor Wake Modelling for High Speed Applications,” Proceedings of the 44th Annual American Helicopter Society Forum, Washington, DC, May 1988.

¹⁸Quackenbush, T. R., Bliss, D. B., and Wachspres, D. A., “Computational Analysis of Hover Performance using a New Free Wake Method,” Presented at the 2nd International Conference on Rotorcraft Basis Research, College Park, MD, February 1988.

¹⁹Johnson, W. R., “Wake Model for Helicopter Rotors in High Speed Flight,” NASA CR-1177507, USAVSCOM TR-88-A-008, November 1988.

²⁰Miller, W. O., and Bliss, D. B., “Direct Periodic Solutions of Rotor Free Wake Calculations,” *Journal of the American Helicopter Society*, Vol. 38, No. 2, April 1993, pp. 53–60.

²¹Crouse, Jr., G. L., and Leishman, J. G., “A New Method for Improved Rotor Free Wake Convergence,” Presented at the 31st AIAA Aerospace Sciences Meeting and Exhibit, Reno, NV, January 1993.

²²Johnson, W., “A General Free Wake Geometry Calculation For Wings and Rotors,” Proceedings of the 51st Annual American Helicopter Society Forum, Fort Worth, TX, May 1995.

²³Bagai, A., and Leishman, J. G., “Rotor Free-Wake Modeling Using a Relaxation Technique - Including Comparisons with Experimental Data,” *Journal of the American Helicopter Society*, Vol. 40, No. 3, July 1995, pp. 29–41.

²⁴Bagai, A., and Leishman, J. G., “Rotor Free-Wake Modeling using a Pseudoimplicit Relaxation Algorithm,” *Journal of Aircraft*, Vol. 32, No. 6, Nov.-Dec. 1995, pp. 1276–1285.

²⁵Bagai, A., and Leishman, J. G., “Free-Wake Analysis of Tandem, Tilt-Rotor and Coaxial Rotor Configurations,” *Journal of the American Helicopter Society*, Vol. 41, No. 3, July 1996, pp. 196–207.

²⁶Bagai, A., and Leishman, J. G., “Adaptive Grid Sequencing and Interpolation Schemes for Rotor Free-Wake Analyses,” *AIAA Journal*, Vol. 36, No. 9, September 1998, pp. 1593–1602.

²⁷Batchelor, G. K., *An Introduction to Fluid Dynamics*, Cambridge University Press, Cambridge, UK, 1967.

²⁸Lamb, H., *Hydrodynamics*, 6th ed. Cambridge University Press, Cambridge, UK, 1932.

²⁹Quackenbush, T. R., Bliss, D. B., and Wachspres, D. A., “New Free Wake Analysis of Rotorcraft Hover Performance Using Influence Coefficients,” *Journal of Aircraft*, Vol. 26, No. 12, December 1990, pp. 1090–1097.

Appendix

The free-vortex wake geometry is a solution to the wake governing equation

$$\frac{\partial \vec{r}}{\partial \psi} + \frac{\partial \vec{r}}{\partial \zeta} = \frac{\vec{V}(\vec{r})}{\Omega} \quad (\text{A-1})$$

The discretized rotor wake problem consists of dividing the curvilinear vortex filaments along their length into a number of straight-line elementary vortex segments, and applying the governing equation at each collocation point on these vortex segments. These equations are then solved numerically by approximating the partial derivatives on the LHS of Eq. A-1 with finite difference approximations.

The velocity source term on the RHS of Eq. A-1 is evaluated by discretizing each vortex filament using a standard straight-line segmentation. The induced velocity is now obtained by exactly integrating the Biot-Savart law for each straight-line vortex segment as

$$\vec{V}_{element} = \frac{\Gamma_v}{4\pi} \frac{h}{(r_c^{2n} + h^{2n})^{1/n}} (\cos \theta_1 - \cos \theta_2) \vec{e} \quad (\text{A-2})$$

Now, the total velocity at a collocation point is evaluated by performing a summation over all the vortex elements. The velocity at the mid-point of a grid cell is obtained by averaging the velocities at the four collocation points of that grid cell.

$$\vec{V} = \frac{1}{4} \left[\vec{V}(\vec{r}(\psi+\Delta\psi, \zeta+\Delta\zeta)) + \vec{V}(\vec{r}(\psi+\Delta\psi, \zeta)) + \vec{V}(\vec{r}(\psi, \zeta+\Delta\zeta)) + \vec{V}(\vec{r}(\psi, \zeta)) \right] \quad (\text{A-3})$$

This averaging procedure is second-order accurate and, therefore, for both the time-marching algorithms the RHS is evaluated up to a second-order accuracy.

Both PCC and PC2B algorithms use a five-point central difference scheme for evaluating the spatial (ζ) derivative. This is given by

$$D_\zeta \vec{r}(\psi + 1/2\Delta\psi, \zeta + 1/2\Delta\zeta) = \quad (\text{A-4})$$

$$\frac{\vec{r}(\psi+\Delta\psi, \zeta+\Delta\zeta) - \vec{r}(\psi+\Delta\psi, \zeta) + \vec{r}(\psi, \zeta+\Delta\zeta) - \vec{r}(\psi, \zeta)}{4\Delta\zeta}$$

The PCC algorithm uses the same scheme for evaluating the temporal derivative, i.e.,

$$D_{\psi}\bar{r}(\psi + 1/2\Delta\psi, \zeta + 1/2\Delta\zeta) \quad (\text{A-5})$$

$$= \frac{\bar{r}(\psi + \Delta\psi, \zeta + \Delta\zeta) - \bar{r}(\psi, \zeta + \Delta\zeta) + \bar{r}(\psi + \Delta\psi, \zeta) - \bar{r}(\psi, \zeta)}{4\Delta\psi}$$

The PC2B algorithm uses a 2nd-order backward difference scheme. The 2nd-backward approximation for the partial derivative at a point $(\psi + 1/2\Delta\psi, \zeta)$ is given by

$$\tilde{D}_{\psi}\bar{r}(\psi + 1/2\Delta\psi, \zeta + 1/2\Delta\zeta) \quad (\text{A-6})$$

$$= \frac{3\bar{r}(\psi + \Delta\psi, \zeta) - \bar{r}(\psi, \zeta) - 3\bar{r}(\psi - \Delta\psi, \zeta) + \bar{r}(\psi - 2\Delta\psi, \zeta)}{4\Delta\psi}$$

The time-integration algorithms can now be constructed using these approximations along with the discretized induced velocity calculations. The PCC algorithm is written in the form

$$(D_{\psi} + D_{\zeta})\bar{r} = \vec{V}(\bar{r}) \Big|_{\bar{r}(\psi + \Delta\psi/2, \zeta + \Delta\zeta/2)} \quad (\text{A-7})$$

where \vec{V} denotes the averaged induced velocity at the cell mid-point $\bar{r}(\psi + \Delta\psi/2, \zeta + \Delta\zeta/2)$, as given by Eq. A-3. Similarly, the PC2B algorithm is given by

$$(\tilde{D}_{\psi} + D_{\zeta})\bar{r} = \vec{V}(\bar{r}) \Big|_{\bar{r}(\psi + \Delta\psi/2, \zeta + \Delta\zeta/2)} \quad (\text{A-8})$$

The five-point central difference approximations used in the PCC have the special property that for equal discretization along ψ and ζ , the truncation errors from the LHS of Eq. A-7 cancel each other. Therefore, the solution accuracy is determined by the second-order accurate evaluation of the RHS velocity terms. The second-order backward difference approximation used in the PC2B scheme results in truncation errors from the LHS of Eq. A-8. However, these errors are of a higher order and the overall solution accuracy is second-order accurate. The additional truncation errors, in particular term dissipative terms, are important in containing the growth of non-physical numerical errors.